RSC Applied Interfaces

ROYAL SOCIETY OF CHEMISTRY

PAPER

View Article Online
View Journal

Cite this: DOI: 10.1039/d5lf00210a

Photoelectrochemical degradation and regeneration of $Ca_2Fe_2O_5$ photocathodes

Louise De Cian, [a] María Isabel Díez-García, [ab] Benjamin Goldman[a] and Kevin Sivula *[a]

$Ca_2Fe_2O_5$ is a p-type semiconductor with properties suitable for potential application as a photocathode in photoelectrochemical water splitting. However, it suffers from poor stability under working conditions that is still not completely understood. In this work, we investigate the degradation mechanism of thermochemically prepared $Ca_2Fe_2O_5$ thin film photoelectrodes and examine the effect of surface protective layers. The magnitude of the sacrificial photocurrent generated by $Ca_2Fe_2O_5$ photocathodes (*ca.* 0.1 mA cm^{-2} under 1 sun) strongly decreases after exposure to electrolyte under applied potential for several hours in the dark, and this decline was not found to be preventable using standard protective overlayers. However, electrochemical and *in situ* UV-vis experiments reveal a dual aspect of the degradation due to both iron reduction and calcium leaching. Kinetically controlling these aspects reveals that a degraded photocathode can be regenerated if only iron reduction occurs but also shows that the degradation is irreversible and leads to a conversion of the $Ca_2Fe_2O_5$ to iron oxide when calcium leaching prevails.

Received 23rd July 2025,
Accepted 8th August 2025

DOI: 10.1039/d5lf00210a

rsc.li/RSCApplInter

Introduction

Considerable attention has been paid to the development of new materials for green hydrogen production *via* photoelectrochemical (PEC) water splitting.[1–3] A suitable semiconductor photoelectrode needs to absorb a large range of the visible spectrum, separate and transport the photogenerated charges, be stable in aqueous solution, and be preferably prepared from earth-abundant elements in a simple synthesis to be affordable and scalable. Semiconductor metal oxides are the prototypical materials investigated for PEC and various n-type metal oxides have been widely investigated as photoanodic materials, with TiO_2,[4,5] Fe_2O_3,[6,7] and $BiVO_4$ (ref. 8 and 9) gaining considerable interest. On the other hand, p-type metal oxides for photocathodes[10] have been less intensively studied, with a focus on copper oxides, such as cuprous oxide (Cu_2O),[11] and delafossite ($CuFeO_2$).[10,12] Recently, various other ternary oxide materials have emerged as promising candidates (*e.g.* $LaFeO_3$,[13] $ZnFe_2O_4$ (ref. 14) and $CuBi_2O_4$ (ref. 15)). While these materials have proper bandgap and energy level position for water (or H^+) reduction, these materials suffer either from poor stability in aqueous solution or from a poor ability to catalyse the hydrogen evolution reaction (HER), requiring addition of protective layers and expensive catalyst. Thus, despite recent efforts, an ideal p-type oxide photocathode material has not been found, which motivates the further exploration of potentially promising materials.

Calcium iron oxide with the atomic formula of $Ca_2Fe_2O_5$ is a p-type semiconductor with a perovskite-like brownmillerite structure ($A_2B_2O_5$),[16] which is orthorhombic and contains alternating layers of BO_6 octahedra and BO_4 tetrahedra[17] typically with oxygen vacancies in the [101] direction of the perovskite unit cell.[18] It has been previously used in Li-ion batteries[19] and catalysis,[20] but it has also an appropriate band gap of 2.0 to 2.2 eV and good band position for PEC water splitting,[21] or other photocatalytic applications.[22–24] Moreover, it is made of earth-abundant elements, suggesting that it could be low-cost and sufficiently scalable for addressing green hydrogen production at significant magnitude. Previous studies have reported that the photocurrent density generated by $Ca_2Fe_2O_5$ photocathodes under standard illumination conditions can reach up to 300 μA cm^{-2},[21,25] which is slightly higher than similar materials.[26,27] However, despite these initial but promising studies, $Ca_2Fe_2O_5$ suffers from a poor stability under working conditions. The degradation has been attributed to photocorrosion creating surface defects and leading to enhanced surface recombination.[28] Previous studies on various other unstable photocathode semiconductors have demonstrated that photocorrosion can be prevented by the addition of a stable wide-band gap metal

[a] *Laboratory for Molecular Engineering of Optoelectronic Nanomaterials, École Polytechnique Fédérale de Lausanne, Station 6, 1015 Lausanne, Switzerland. E-mail: kevin.sivula@epfl.ch*
[b] *Catalonia Institute for Energy Research (IREC), Jardins de les Dones de Negre 1, 08930 Sant Adrià del Besòs, Barcelona, Spain*

oxide as a protective overlayer.[29] However, to the best of our knowledge, this strategy has not been reported for application to $Ca_2Fe_2O_5$. Among the various deposition strategies for protecting overlayers, atomic layer deposition (ALD) has emerged as the most effective and reproducible technique. Using ALD, a precise thickness control and a uniformly distributed layer can be achieved,[30–32] making this a promising technique to afford stability to a wide variety of materials for PEC application.

In this work, we investigate the photocathodic performance deterioration of thermochemically prepared $Ca_2Fe_2O_5$ photocathodes under different conditions and examine the possibility to stabilize this material through the deposition of a stable wide-band gap metal oxide as a protective layer using ALD. We discuss the partial regeneration of the material observed when the degradation process is stopped at an early stage and compare it to the effects of an advanced and irreversible deterioration. Finally, we propose an explanation for the degradation of $Ca_2Fe_2O_5$.

Results and discussion

The $Ca_2Fe_2O_5$ electrodes used in this study were synthesized using a two-step technique, based on the work of Yoon *et al.*[21] The first step is the formation of a nanostructured FeOOH film on F-doped SnO_2 coated glass substrates (FTO glass) using a hydrothermal method. The second step is the conversion of FeOOH to $Ca_2Fe_2O_5$ *via* a solid-state reaction (at 620 °C for 2 hours) with excess $Ca(NO_3)_2$ drop-casted from DMF solution. Residual surface impurities were removed with acetic acid to obtain a pure brownmillerite phase film on FTO. Fig. 1a shows the XRD pattern of a typical $Ca_2Fe_2O_5$ film where the peaks corresponding to FTO are marked with stars. A large bump expands from 2θ = 10 to 40°, suggesting a degree disorder potentially due to the formation of an amorphous phase of calcium iron oxide. Nevertheless, all the brownmillerite characteristic peaks are present (see peak labels in Fig. 1a), and no impurity phases are observed. The formation of $Ca_2Fe_2O_5$ was further confirmed by Raman spectrometry (Fig. 1b). The main modes at 254, 290, 379, 427, 555 and 706 cm^{-1} assigned to the A_g symmetry correspond to the internal vibration modes of FeO_6 octahedra.[33] Scanning electron microscope (SEM) images (Fig. 1c–e) show the top-down film morphology of the starting FeOOH nanorods (Fig. 1c) and the resulting $Ca_2Fe_2O_5$ nanoflakes (Fig. 1d). The thin and mostly vertically organized FeOOH nanorods were converted into large and randomly oriented flakes. A cross-section SEM image (Fig. 1e) of the $Ca_2Fe_2O_5$ film shows the *ca.* 1 μm thick layer nanosheets on top of the *ca.* 400 nm thick FTO

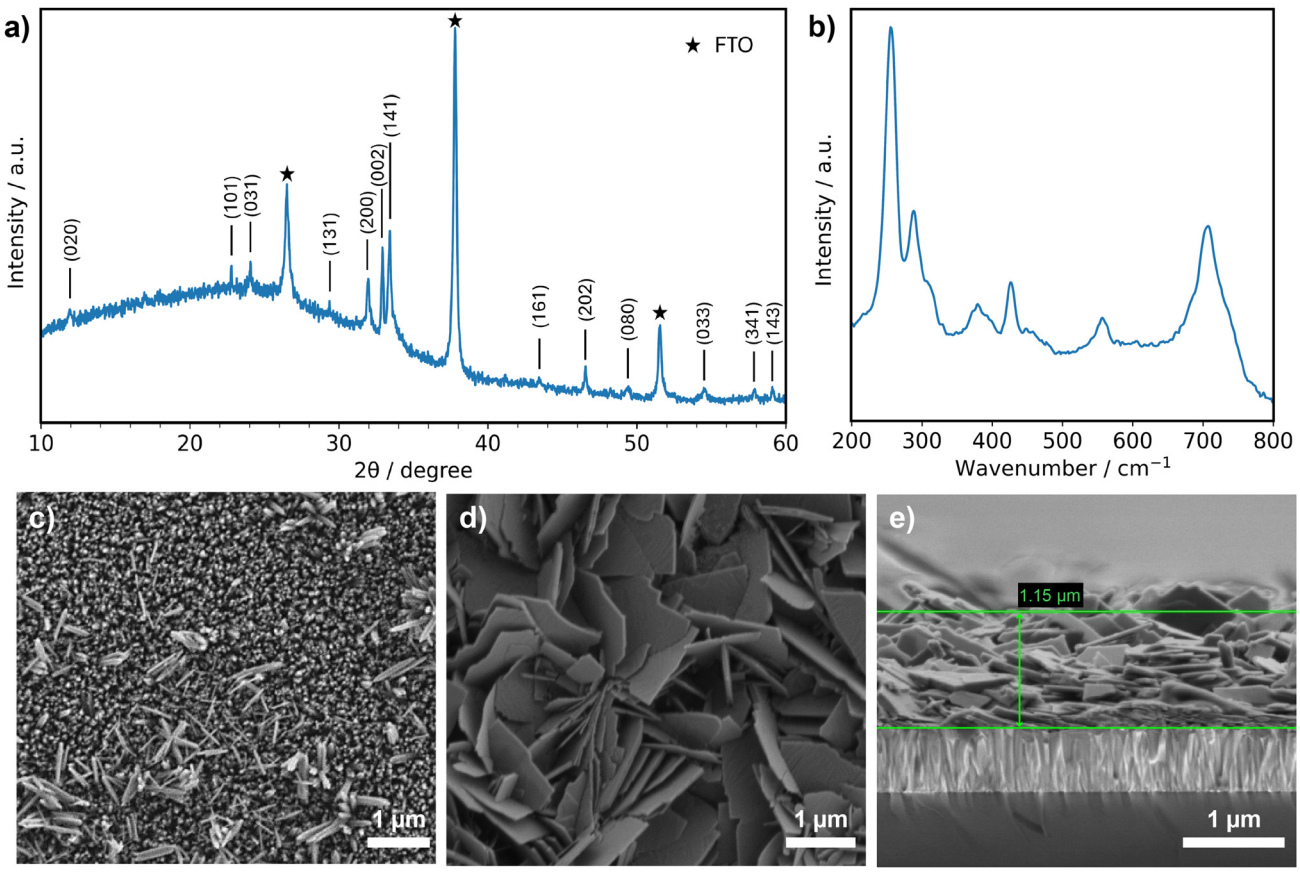

Fig. 1 a) XRD pattern of $Ca_2Fe_2O_5$. The (*hkl*) indices are based on JCPDS No. 47-1744. b) Raman spectrum of $Ca_2Fe_2O_5$. SEM images of c) FeOOH nanorods, d) $Ca_2Fe_2O_5$ nanoflakes, e) cross-section of $Ca_2Fe_2O_5$ deposited on FTO glass.

layer and confirms the complete conversion of FeOOH to $Ca_2Fe_2O_5$.

As the degradation of $Ca_2Fe_2O_5$ was previously attributed to light exposure (photodegradation), this aspect was tested by subjecting the photoelectrodes to illumination and applied potential separately in comparison to a pristine control sample. A first photoelectrode was immersed in aqueous electrolyte (borate buffer pH 11, since this was previously demonstrated as the most suitable environment for $Ca_2Fe_2O_5$ (ref. 28)) and illuminated with a 1000 W xenon lamp for 18 h without any external electrical connection. In contrast, a potential of +0.65 V *vs.* the reversible hydrogen electrode (RHE) was applied for 18 h on a second photoelectrode immersed in the same electrolyte under strictly dark conditions. For this latter electrode a total charge of *ca.* 12 mC cm^{-2} passed during the first 3 hours application of potential, wherein the majority of the charge passed during the first 15 minutes (see Fig. S1, SI). As shown in Fig. 2a, an obvious colour change was observed for the photoelectrode exposed to the applied potential in the dark, likely due to the reduction of Fe^{3+} to Fe^{2+}. This colour change was assessed *via* UV-vis spectrophotometry using an integrating sphere to account for the strong scattering of the electrodes (see Kubelka–Munk plots in Fig. S2, SI). Despite the colour change observable with naked eye, UV-vis spectra are very similar and the estimated band gaps are the same at 2.4 eV. We note that the colour of the illuminated electrode was similar to the pristine control electrode.

The PEC performance of the $Ca_2Fe_2O_5$ photoelectrodes was evaluated in aqueous 0.5 M borate buffer (pH 11) with the addition of 0.5 M $Na_2S_2O_8$ as a sacrificial electron scavenger, to decouple the desired characterization of the photogenerated carrier extraction from the HER catalysis.[34] Assessment of the photogenerated charge extraction was conducted using linear scanning voltammetry (LSV) under intermittent illumination conditions (1 sun) on photoelectrodes subjected to the same conditions shown in Fig. 2a. Typical LSV curves are shown in Fig. 2b. The photogenerated current density was observed to be approximately the same for the pristine control sample and the sample exposed to extended illumination conditions, with a current density of 85 and 79 μA cm^{-2} at +0.5 V *vs.* RHE, respectively. However, the current density recorded for the electrode exposed to a potential of +0.65 V *vs.* RHE was six times smaller, with a current density of only 13 μA cm^{-2} recorded at +0.5 V *vs.* RHE. This observation strongly indicates that photocorrosion is not the dominant cause of instability of the material under operation, since there was a clear degradation of the material in the dark when applying a potential, but not when only exposed to light.

While the photocorrosion explanation for the poor stability proposed in previous work is not supported by this initial demonstration, more analyses remain required to better explain the degradation processes of $Ca_2Fe_2O_5$ under applied potential. Interestingly, the duration of exposure to a potential does not seem to influence the bulk characteristics of $Ca_2Fe_2O_5$. The crystallinity and Raman spectrum of the material exposed to +0.65 V *vs.* RHE between 10 minutes and 10 hours do not vary from the pristine $Ca_2Fe_2O_5$ (Fig. S3, SI), implying a slight modification of the material that must occur only at the surface of the film. Moreover, we observed that $Ca_2Fe_2O_5$ photocathodes that had undergone the extended potential treatment in the dark (and become discoloured as a result) turned back to their original/pristine colour after exposure to ambient conditions in air for several days, suggesting a reoxidation of reduced iron atoms (see photoelectrode photographs in Fig. S4, SI). This aspect complicates attempts to quantify the amount of reduced iron atoms in these film by photoelectron spectroscopy, however, attempts to facilitate the re-oxidation process by subjecting

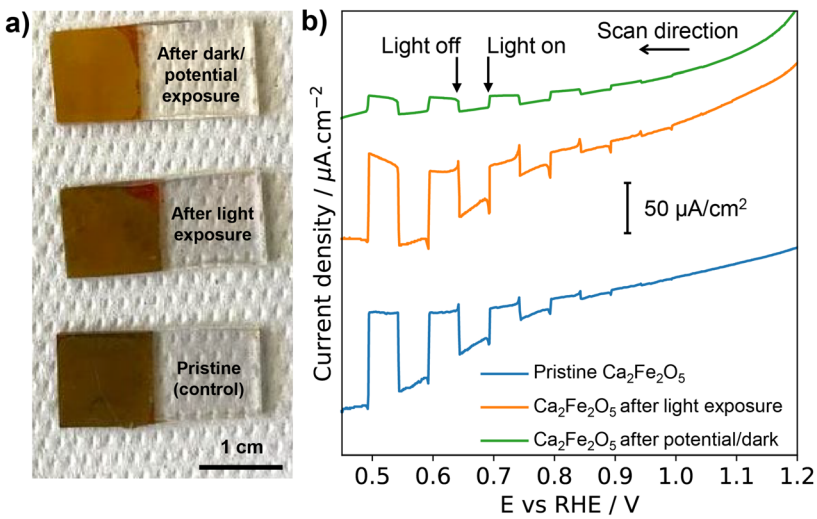

Fig. 2 a) Photographs of photoelectrodes: from bottom to top are the control sample, after 18 hours exposed to light in borate buffer pH 11, and after 18 hours exposed to +0.65 V *vs.* RHE in borate buffer pH 11. b) LSV curves (scan rate 10 mV s^{-1}) under intermittent illumination conditions recorded for the three samples in borate buffer pH 11 plus 0.5 M $Na_2S_2O_8$.

"reduced" photocathodes to a "regenerating" thermal treatment for 2 hours at 620 °C (based on the synthesis conditions) revealed two distinct outcomes depending on the duration of the exposure of the $Ca_2Fe_2O_5$ to PEC testing conditions.

When chronoamperometry (CA) measurements were performed at a potential of +0.5 V *vs.* RHE for 16 hours under illumination, the resulting "reduced" orange material turned red after thermal regeneration treatment for 2 hours at 620 °C. The UV-vis spectrum and a photograph of the resulting red film (after CA treatment and regeneration) are shown in Fig. 3a compared to a pristine $Ca_2Fe_2O_5$ photoelectrode. The shape of the UV-vis spectrum clearly changes with a small shoulder appearing around 550 nm, suggesting the formation of a new phase. The performance of this "CA/regenerated" photoelectrode was significantly decreased with a 1-sun photocurrent density of <5 μA cm^{-2} (see LSV in Fig. S5, SI). On the other hand, when only LSV measurements (from +1.25 V to +0.45 V *vs.* RHE with a sweeping rate of 10 mV s^{-1}) are performed on a pristine $Ca_2Fe_2O_5$ photocathode under intermittent illumination (considerably decreasing the duration of exposure to potential compared to the CA treatment) the similarly orange-coloured electrode that results turns back to its original brown colour after thermal regeneration treatment as indicated by the UV-vis spectrum for the "LSV/regenerated" sample in Fig. 3a, which is almost identical to the pristine $Ca_2Fe_2O_5$ sample. It should be noted that before the thermal regeneration treatment photoelectrodes that underwent LSV testing showed a slight reduction of visible light absorbance (see Fig. S6, SI) that was restored upon the regeneration treatment. Further analysis by X-ray diffraction (XRD, Fig. 3b) and grazing incidence XRD (Fig. 3c) give further insight into the change of crystal phase in the two cases of CA/regeneration and LSV/regeneration. The XRD patterns of the samples after regeneration treatment indicate a loss of crystallinity in the CA/Regenerated film, with a decrease in the intensity of all peaks corresponding to $Ca_2Fe_2O_5$ relative to the FTO substrate, and the appearance of a weak new peak at *ca.* 2θ = 35.6°. Grazing incidence XRD (ω = 0.5°) was used to help identify the new phase in this sample since the incident X-rays probe more selectively the top of the film, reducing reflections from the FTO underlayer. By comparing the pristine $Ca_2Fe_2O_5$ photoelectrode to the CA/regenerated film the $Ca_2Fe_2O_5$ phase can still be distinguished, but two new peaks appear *ca.* 35.6° and 40.8° characteristic of hematite (α-Fe_2O_3). Within the resolution of the grazing incidence XRD measurement, fitting the data shows a significant fraction of hematite with an approximate Fe_2O_3 : $Ca_2Fe_2O_5$ ratio of 1.3 : 1 (see the pattern sub-fits in Fig. S7, SI). The Raman spectrum of the CA/Regenerated film also confirms the presence of hematite with two characteristic peaks appearing at 225 and 610 cm^{-1} (Fig. S8, SI). In contrast with the CA/regenerated films the LSV/regenerated films retained their characteristic $Ca_2Fe_2O_5$ phase reflections (despite a noticeable decrease in the (002) peak at 33°, which will be discussed later), suggesting that the brownmillerite structure

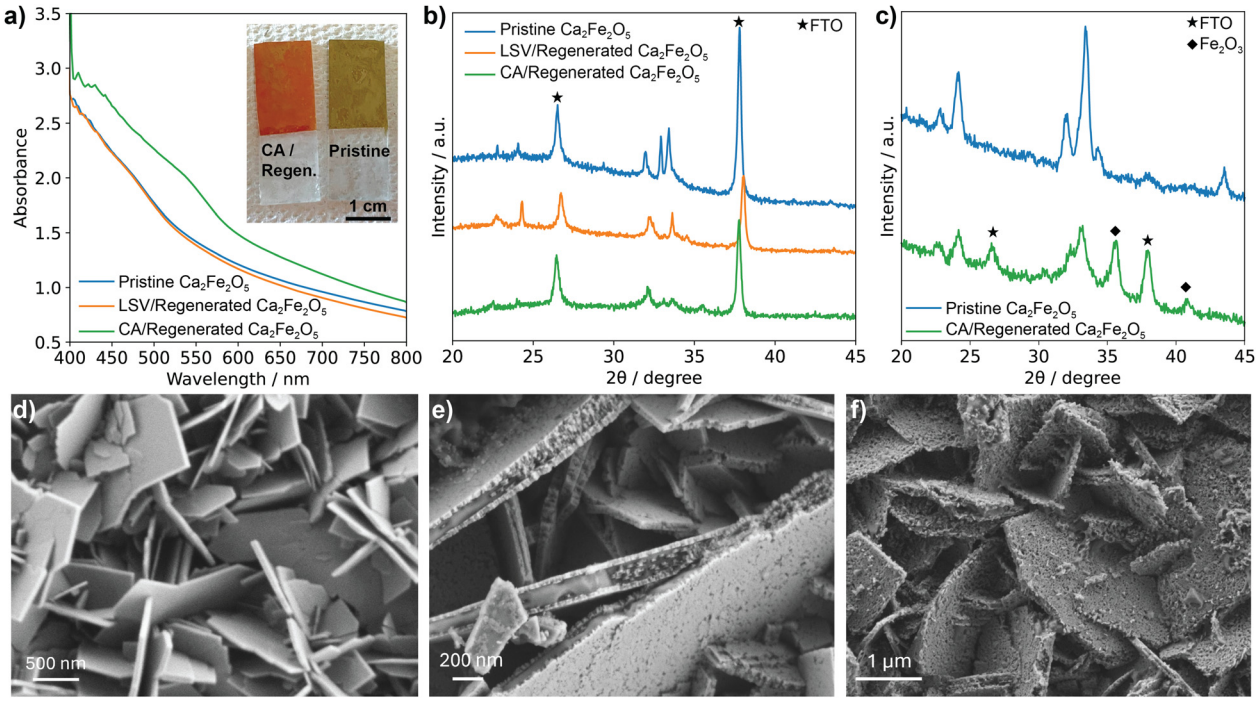

Fig. 3 a) UV-vis absorption spectra of CA and LSV treated films followed by the thermal regeneration treatment as compared to a pristine $Ca_2Fe_2O_5$ film. The inset shown a photograph of the CA/regenerated film compared to the pristine. b) XRD patterns of the films from (a). c) Grazing-incidence XRD pattern (ω = 0.5°) of the pristine $Ca_2Fe_2O_5$ and CA/regenerated film. For (b) and (c) the FTO peaks are labelled as stars. Top-down SEM images of d) pristine $Ca_2Fe_2O_5$, e) LSV/regenerated, and f) CA/regenerated films are also shown.

is retained during the LSV-regeneration process. Furthermore, the grazing incidence XRD of LSV and CA films that were not regenerated did not present any additional peaks compared to the pristine film, supporting that only the regeneration of the strongly degraded films leads to hematite formation (Fig. S9, SI).

Analysis of the films by XPS gives further insight into to the degradation, despite the aforementioned difficulty in quantifying the oxidation states due to reoxidation of the surface after electrochemical testing. When comparing the XPS spectra of Fe 2p for pristine and CA/regenerated $Ca_2Fe_2O_5$, a strong peak corresponding to Sn 3p overlaps with Fe 2p peaks of regenerated $Ca_2Fe_2O_5$ (Fig. S10a) likely due to the increased contribution of FTO to the XPS spectra due to the corrosion of the material.

To get a better understanding of the degradation mechanism in both LSV/ and CA/regeneration cases, the resulting samples were observed with SEM. Compared to the pristine $Ca_2Fe_2O_5$, which is shown at a higher zoom in Fig. 3d, the $Ca_2Fe_2O_5$ in the LSV/regenerated films (Fig. 3e) appear to show a sandwich-type structure where the basal planes of the sheets have a porous crust with a thickness of *ca.* 40 nm. The preferential conversion of the basal plane observed in this case, due to the sheet-type morphology of the $Ca_2Fe_2O_5$ suggests a reasonable explanation for the preferential decrease in the (002) reflection. Similarly, the CA/regenerated film (Fig. 3f) shows increased porosity through the entire thickness of the sheet and a fully damaged structure. Using energy-dispersive X-ray spectroscopy, we observed that the calcium weight fraction significantly decreased for CA/regenerated film with a Fe : Ca ratio of 1 : 0.44, compared to 1 : 0.9 for LSV/regenerated films. The loss of calcium in the film was supported by the detection of 0.58 μg mL^{-1} of calcium in the electrolyte, revealed by ICP-MS, compared to only 0.04 μg mL^{-1} of iron. XPS also supports these observations. When comparing the XPS spectra of Ca 2p for pristine, light-exposed and potential-exposed $Ca_2Fe_2O_5$ samples, with deconvolution of the peaks to measure the relative proportion of Ca in a chemical environment consistent with CaO or $Ca_2Fe_2O_5$ as shown in Fig. S10b–d, respectively, it appears that the relative amount of Ca in $Ca_2Fe_2O_5$ decreases only slightly with light exposure, but decreases more drastically with exposure to potential. Moreover, when comparing the relative atomic proportions of Ca and Fe measured by their respective XPS 2p peaks for pristine, light-exposed and potential exposed $Ca_2Fe_2O_5$ samples we see a similar trend (see Table S1, SI) where the amount of Ca decreases drastically with the potential treatment. These observations not only confirm the view that photocorrosion is not the dominant cause of instability of the material under operation, but suggest that the surface of the material disproportionates upon electrochemical testing, which can lead to the leaching of Ca into the electrolyte.

From these observations, we can reasonably conclude that calcium leaching is initiated by iron reduction and the material disproportionation when applying a potential during PEC measurement. However, we hypothesized that the two processes of iron reduction and calcium leaching occur on different time scales. Indeed, in the case of the CA/regenerated photocathodes significant leaching occurs and regenerating the films leads to a large proportion of Fe_2O_3 formation, however the comparatively brief exposure of the $Ca_2Fe_2O_5$ to the PEC testing conditions in the LSV-tested film causes iron reduction by avoiding significant Ca leaching. This leads to an interesting effect in the PEC performance of LSV/regenerated photocathodes as shown by plotting the magnitude of the 1-sun photocurrent density at +0.47 V *vs.* RHE observed after subsequent LSV measurements and regeneration cycles as shown in Fig. 4. Initially, the pristine photocathode shows a decrease in photocurrent after each LSV cycle, likely due to the reduction of the iron, after each regeneration cycle, and after 5 LSVs only *ca.* 10 μA cm^{-2} was produced compared to the initial performance of *ca.* 40 μA cm^{-2}. However, thermally regenerating this photocathode enhanced the photocurrent to >50 μA cm^{-2} and 5 subsequent LSVs showed a drop to only *ca.* 40 μA cm^{-2} (Fig. 4, second panel). This LSV-regeneration cycle can be repeated several times, with only small decrease of the maximum photocurrent density observed but an improved stability.

Combined, the presented data support the view that, when the exposure to PEC measurement conditions is short, the calcium loss is negligible and $Ca_2Fe_2O_5$ can be partially regenerated with the thermal treatment. Based on the SEM images in Fig. 3, a thin layer of iron oxide is formed on the surface of the $Ca_2Fe_2O_5$ sheets, slightly reducing the photocurrent but improving the stability by protecting the underlying $Ca_2Fe_2O_5$. Nevertheless, it should be noted that the energy levels of hematite are not suitable for H_2 production *via* water reduction, so while there may be photocurrent due to the sacrificial $Na_2S_2O_8$ included in the PEC measurement, the hematite protection strategy is not suitable for photocathodic H_2 production. Conversely, when the potential is applied for longer, the calcium leakage becomes significant, and the thermal regeneration yields a large proportion of hematite, preventing the charge transport between $Ca_2Fe_2O_5$ and the electrolyte. We note that photocathodes were tested in electrolyte saturated with $Ca(OH)_2$, but these conditions did not prevent calcium leaching.

While the *in situ* grown hematite protection layer is not suitable, as demonstrated for many previous semiconductor photoelectrodes, the correct choice of a protecting overlayer can limit corrosion reactions and still allow H_2 prodution.[29] Accordingly, we tried to stabilize the material with the addition of surface protective layers to avoid direct contact with the electrolyte and degradation *via* leakage of one of the elements. Following the procedure established by Pan *et al.*,[35] two different protective layers were deposited using atomic layer deposition (ALD): a 20 nm TiO_2 layer, and a 20 nm Ga_2O_3 layer with a 20 nm TiO_2 layer on top. Platinum was

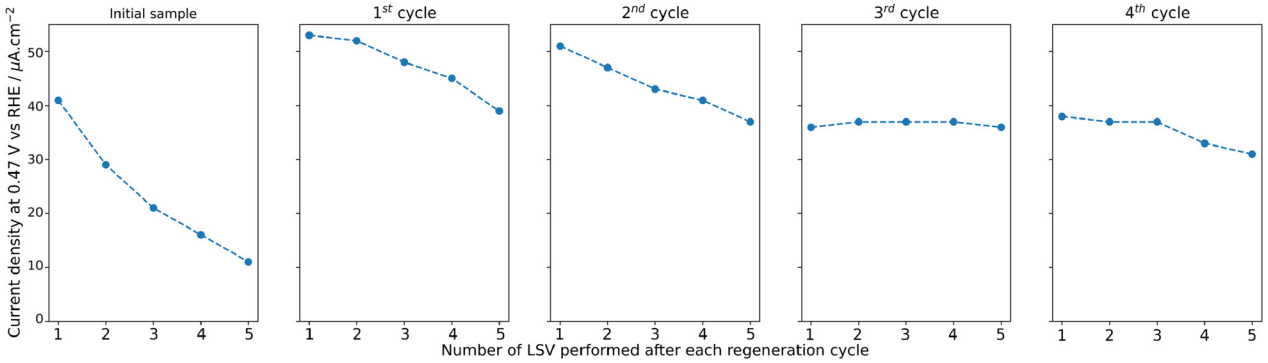

Fig. 4 Evolution of the current density at +0.47 V *vs.* RHE as a function of the number of LSV performed in borate buffer pH 11, after each regeneration cycle.

then photodeposited on the electrodes as a co-catalyst for H_2 production, following the work of Caretti *et al.*[36]

The photocurrent generated by the resulting electrodes was very low (*ca.* 0.6 μA cm^{-2} recorded at +0.5 V *vs.* RHE for Ga_2O_3 and TiO_2, see LSVs in Fig. S11, SI), indicating either an improper band alignment or, more likely, a partial degradation of $Ca_2Fe_2O_5$ during the overlayer deposition process as the electrodes turned light-orange after ALD. An inversion from photocathodic to photoanodic current is also visible above +1.0 V *vs.* RHE. This observation further supports the degradation of $Ca_2Fe_2O_5$ during ALD.

However, CA was performed at +0.65 V *vs.* RHE for one hour and the current density observed was more stable than for the unprotected film (Fig. S12, SI). This encouraging result suggests that an improvement of the stability is possible using overlayers, but more work is required to find an overlayer material with a suitable band alignment between $Ca_2Fe_2O_5$ and the protection layer and suitable deposition conditions to preserve underlying semiconducting material.

Conclusions

We demonstrated that $Ca_2Fe_2O_5$ exhibits considerable photostability, even when subjected to aqueous conditions under 1-sun illumination for extended time. However, when applying a modest potential, suitable for typical photocathode operation, even in the dark $Ca_2Fe_2O_5$ appears to suffer from the reduction of iron atoms and the leaching of calcium atoms into the electrolyte. However, we showed that $Ca_2Fe_2O_5$ can be partially regenerated depending on the duration of the exposure to applied potential. If the exposure is stopped at an early stage, calcium loss is negligible in the bulk and the photocurrent can be recovered by thermal regeneration treatment leaving a thin layer of iron oxide formed on the surface, which enhances the stability of the photoelectrochemical operation (under sacrificial reduction conditions). On the other hand, after extended duration (chronoamperometry) testing of $Ca_2Fe_2O_5$, when the calcium leaching is significant, a substantial amount of Fe_2O_3 is formed after thermal regeneration, and the loss of photoelectrochemical performance becomes irreversible. This phenomenon cannot be prevented by saturation of the electrolyte with Ca ions. Moreover, while the observed stability granted by a thin *in situ*-grown Fe_2O_3 overlayer gives promise to the overlayer protection strategy, the deposition of classic surface protection layers *via* ALD, as TiO_2 and Ga_2O_3, were not successful presumably due to the deterioration of the $Ca_2Fe_2O_5$. We believe that optimizing the overlayer deposition conditions and the band alignment of the materials could be a fruitful path to effectively protect the material, enabling it for development as a photocathode for solar H_2 production.

Experimental

Materials

Iron(III) chloride ($FeCl_3{\cdot}6H_2O$, 97%), calcium(II) nitrate ($Ca(NO_3)_2{\cdot}4H_2O$, 99%) were purchased from Alfa Aeser. Sodium nitrate ($NaNO_3$, ≥99%), boric acid ($B(OH)_3$, 99.6%) were purchased from Acros Organics. Acetic acid (CH_3COOH, 99.7%) was purchased from Chemie Brunschwig AG. Sodium persulfate ($Na_2S_2O_8$, 99.0%) was purchased from Sigma Aldrich. Potassium hydroxide (KOH, 85%) was purchased from Carlo Erba.

Synthesis of $Ca_2Fe_2O_5$

Fluorine-doped tin oxide (FTO) coated aluminiumborosilicate glass (3 × 1.3 cm), Solaronix S.A., was cleaned by sequential sonication in distilled water, ethanol and acetone for 20 minutes. FeOOH films were synthesized on FTO glass using a hydrothermal method. A 250 mL aqueous solution of $FeCl_3{\cdot}6H_2O$ (10 g, 0.148 M) and $NaNO_3$ (21.25 g, 1 M) was prepared and aged for one day. The samples were immersed in the iron solution, tightly sealed in a glass container, and placed in an oven at 100 °C for 6 hours. At the end of the synthesis, the container was allowed to slowly cool to rt over 1 h. The FTO substrates were removed from the opaque solution, rinsed with distilled water, and then dried on a hot plate at 50 °C in air. For the thermochemical conversion process, 200 μL of a 50 mM $Ca(NO_3)_2{\cdot}4H_2O$ solution in dimethylformamide (DMF) were drop-casted on the FeOOH film on a hot plate at 110 °C. Then, the samples were placed

in a pre-heated furnace at 140 °C. The temperature was increased to 620 °C at a rate of 8 °C min^{-1} (2 h dwell), followed by a slow cooling to rt. The samples were immersed in a 0.5 M acetic acid solution for 30 minutes at 0 °C using an ice bath to remove the grey shiny layer of calcium oxide that covered the material. The resulting electrodes were rinsed with distilled water and dried on a hot plate at 50 °C. The final $Ca_2Fe_2O_5$ films were brown in colour.

Basic characterization

Crystallinity was assessed by X-ray diffraction (XRD; Bruker D8 Discover Vario) and grazing incidence diffraction (GID; Bruker D8 Discover Plus TXS) at ω = 0.5°. UV-vis absorption spectra were recorded using a Lambda 365 UV-vis spectrophotometer (Perkin Elmer). Raman spectra were obtained with a LabRam confocal Raman spectrometer (HORIBA Jobin Yvon XploRA PLUS) using a 532 nm wavelength laser. The morphological changes were observed with a scanning electron microscope (SEM; Zeiss Merlin). Elemental analysis was performed on an inductively coupled plasma mass spectrometer Nexlon 350 (ICP-MS; Perkin Elmer).

Photoelectrochemical measurements

The PEC measurements were performed in a three-electrode configuration using a cappuccino cell[37] and a SP-200 potentiostat (BioLogic). The active area of the working electrode was 0.245 cm^2. A carbon counter electrode and an Ag|AgCl (saturated) reference electrode were used. Solar illumination was simulated with a 1000 W xenon lamp and AM 1.5G filter. To convert the potential from *vs.* Ag|AgCl to *versus* the reversible hydrogen electrode (RHE), the following equation was used:

$$E_{RHE} = E_{Ag|AgCl} + E^0_{Ag|AgCl} + 0.059 \times pH$$

where $E^0_{Ag|AgCl}$ = 0.197 V for a saturated KCl solution at 25 °C.

All measurements were performed in 0.5 M borate buffer adjusted to pH 11 using KOH, containing 0.5 M of $Na_2S_2O_8$ as a sacrificial agent. Linear scanning voltammetry (LSV) curves were recorded under chopped illumination while scanning the potential at a rate of 10 mV s^{-1} from +1.25 V to +0.45 V *vs.* RHE.

Conflicts of interest

There are no conflicts to declare.

Data availability

Fig. S1–S12 described in the main text. See DOI: **https://doi.org/10.1039/D5LF00210A**.

Data for this article, including data used to plot Fig. 1a and b, 2b, 3a–c, 4, S1, S3, and S5 are available at **http://zenodo.org** at **https://doi.org/10.5281/zenodo.14823908**.

Acknowledgements

This publication was created as part of NCCR Catalysis (grant number 180544), a National Centre of Competence in Research funded by the Swiss National Science Foundation.

Notes and references

1 Z. Li, S. Fang, H. Sun, R. Chung, X. Fang and J. He, *Adv. Energy Mater.*, 2023, **13**, 2203019.
2 H. Song, S. Luo, H. Huang, B. Deng and J. Ye, *ACS Energy Lett.*, 2022, 1043–1065.
3 K. Sivula and R. van de Krol, *Nat. Rev. Mater.*, 2016, **1**, 15010.
4 R. V. Nair, V. S. Gummaluri, M. V. Matham and V. C, *J. Phys. D: Appl. Phys.*, 2022, **55**, 313003.
5 X. Zhang, S. Zhang, X. Cui, W. Zhou, W. Cao, D. Cheng and Y. Sun, *Chem. – Asian J.*, 2022, **17**, e202200668.
6 K. Sivula, F. Le Formal and M. Grätzel, *ChemSusChem*, 2011, **4**, 432–449.
7 Y. W. Phuan, W.-J. Ong, M. N. Chong and J. D. Ocon, *J. Photochem. Photobiol., C*, 2017, **33**, 54–82.
8 J. H. Kim and J. S. Lee, *Adv. Mater.*, 2019, **31**, 1806938.
9 T. W. Kim and K.-S. Choi, *Science*, 2014, **343**, 990–994.
10 Y. J. Jang and J. S. Lee, *ChemSusChem*, 2019, **12**, 1835–1845.
11 I. V. Bagal, N. R. Chodankar, M. A. Hassan, A. Waseem, M. A. Johar, D.-H. Kim and S.-W. Ryu, *Int. J. Hydrogen Energy*, 2019, **44**, 21351–21378.
12 Q.-L. Liu, Z.-Y. Zhao, R.-D. Zhao and J.-H. Yi, *J. Alloys Compd.*, 2020, **819**, 153032.
13 M.-K. Son, H. Seo, M. Watanabe, M. Shiratani and T. Ishihara, *Nanoscale*, 2020, **12**, 9653–9660.
14 S. Kim, M. A. Mahadik, W.-S. Chae, J. Ryu, S. H. Choi and J. S. Jang, *Appl. Surf. Sci.*, 2020, **513**, 145528.
15 S. A. Monny, L. Zhang, Z. Wang, B. Luo, M. Konarova, A. Du and L. Wang, *J. Mater. Chem. A*, 2020, **8**, 2498–2504.
16 G. J. Redhammer, G. Tippelt, G. Roth and G. Amthauer, *Am. Mineral.*, 2004, **89**, 405–420.
17 T.-L. Phan, N. Tran, D. H. Kim, P. T. Tho, B. T. Huy, T. N. Dang, D.-S. Yang and B. Lee, *J. Am. Ceram. Soc.*, 2018, **101**, 2181–2189.
18 E. Asenath-Smith, I. N. Lokuhewa, S. T. Misture and D. D. Edwards, *J. Solid State Chem.*, 2010, **183**, 1670–1677.
19 N. Sharma, K. M. Shaju, G. V. Subba Rao and B. V. R. Chowdari, *Electrochim. Acta*, 2004, **49**, 1035–1043.
20 A. Kawashima, K. Matsubara and K. Honda, *Bioresour. Technol.*, 2008, **99**, 3439–3443.
21 J.-S. Yoon, Y.-M. Kim, J.-W. Lee and Y.-M. Sung, *Appl. Surf. Sci.*, 2022, **589**, 153012.
22 Y.-H. Chang, W.-C. Tseng, C.-C. Kaun, Y.-H. Su and J.-J. Wu, *ACS Sustainable Chem. Eng.*, 2022, **10**, 12651–12658.
23 D. S. Vavilapalli, L. Qin, J. Palisaitis and J. Rosen, *npj Clean Water*, 2024, **7**, 41.
24 S. Benallal, S. Boumaza, R. Brahimi and M. Trari, *J. Solid State Electrochem.*, 2022, **26**, 1541–1547.
25 Y.-M. Kim, M.-S. Kang, M.-S. Kim and Y.-M. Sung, *Appl. Surf. Sci.*, 2025, **681**, 161437.

26 J. Cao, T. Kako, P. Li, S. Ouyang and J. Ye, *Electrochem. Commun.*, 2011, **13**, 275–278.
27 S. Ida, K. Yamada, T. Matsunaga, H. Hagiwara, Y. Matsumoto and T. Ishihara, *J. Am. Chem. Soc.*, 2010, **132**, 17343–17345.
28 G. P. Wheeler and K.-S. Choi, *ACS Appl. Energy Mater.*, 2018, **1**, 4917–4923.
29 D. Bae, B. Seger, P. C. K. Vesborg, O. Hansen and I. Chorkendorff, *Chem. Soc. Rev.*, 2017, **46**, 1933–1954.
30 A. Paracchino, V. Laporte, K. Sivula, M. Grätzel and E. Thimsen, *Nat. Mater.*, 2011, **10**, 456–461.
31 W. Septina, R. R. Prabhakar, R. Wick, T. Moehl and S. D. Tilley, *Chem. Mater.*, 2017, **29**, 1735–1743.
32 J. Azevedo, S. D. Tilley, M. Schreier, M. Stefik, C. Sousa, J. P. Araújo, A. Mendes, M. Grätzel and M. T. Mayer, *Nano Energy*, 2016, **24**, 10–16.
33 A. Piovano, M. Ceretti, M. R. Johnson, G. Agostini, W. Paulus and C. Lamberti, *J. Phys.:Condens. Matter*, 2015, **27**, 225403.
34 F. Boudoire, Y. Liu, F. Le Formal, N. Guijarro, C. R. Lhermitte and K. Sivula, *J. Phys. Chem. C*, 2021, **125**, 10883–10890.
35 L. Pan, J. H. Kim, M. T. Mayer, M.-K. Son, A. Ummadisingu, J. S. Lee, A. Hagfeldt, J. Luo and M. Grätzel, *Nat. Catal.*, 2018, **1**, 412–420.
36 M. Caretti, L. Lazouni, M. Xia, R. A. Wells, S. Nussbaum, D. Ren, M. Grätzel and K. Sivula, *ACS Energy Lett.*, 2022, **7**, 1618–1625.
37 *Photoelectrochemical Hydrogen Production*, ed. R. Van De Krol and M. Grätzel, Springer US, Boston, MA, 2012, vol. 102.